Available online at www.sciencedirect.com

SciVerse ScienceDirect

Procedia Engineering 58 (2013) 117 – 126

Procedia Engineering

www.elsevier.com/locate/procedia

The Shock and Spall Response of Kovar

Neel, C.H.[a,*], Chhabildas, L.C.[a], Abrahams, R.A.[a]

[a]*Air Force Research Laboratory, Eglin AFB, FL 32542*

Abstract

The shock response and spall strength of Kovar®, an alloy of Fe-29Ni-17Co, are obtained using a single stage powder gun to achieve pressures between 6 and 55 *GPa* by performing symmetric, planar impact tests. Above ~ 6.5 *GPa*, the behavior shifts from a dispersive, continuous pressure rise to a shock, and it is shown that the material displays anomalous behavior at low pressures. Above 6.5 *GPa*, the Hugoniot is described by a linear relationship between shock and particle velocity of $U_S = 2.06U_P + 3.54km/s$. The spall strength, an engineering description of the spall phenomenon, was calculated and shown to increase from 3.6-7.4 *GPa* as stress increases from 6-55 *GPa*, and it is shown that the method of spall strength computation has a large effect. From previous studies on the iron-nickel system, the authors expected to observe evidence of an $\alpha \rightarrow \epsilon$ phase transition in the material but did not. Upon examining the shock and metallurgical literature, high concentrations of Ni and Co will have competing effects on the phase transition, but the effect of Ni will likely dominate and decrease the phase transition pressure. Further experiments on the high alloy Fe-Ni-Co system are needed to understand Kovar's complex low pressure mechanical behavior.

Keywords: kovar, spall, hugoniot, shock

1. Introduction

Iron and iron alloys are among the materials whose mechanical shock response is best characterized and understood. This is unsurprising, due to their ubiquity. However, that ubiquity has lead to a tremendous number of alloys formulated for specific applications. One of the many applications is to match the thermal coefficient of expansion of ceramics and glasses in order to enable hermetic seals in packaged electronics. Kovar®, an Fe-Ni-Co alloy, is used for this purpose, and therefore also finds use in military applications where the high pressure response is important.

Presently, the shock response of Kovar has only been investigated at pressures up to 6 *GPa* [1]. However, a need exists to extend understanding of the shock response to higher pressures. Furthermore, Kovar provides a high alloy dataset from which to examine the effect of Ni and Co on the 13 *GPa*, pressure-induced α (bcc) $\rightarrow \epsilon$ (hcp) phase transformation in iron and iron alloys ([2, 3]). This study investigates the shock behavior of Kovar using parallel plate, normal impact experiments performed using a single stage powder gun. In addition to reporting a Hugoniot and spall strength, we speculate on the reasons for the absence of the expected pressure-induced phase transition.

*Corresponding author
Email address: christopher.neel@eglin.af.mil (Neel, C.H.)

doi:10.1016/j.proeng.2013.05.015

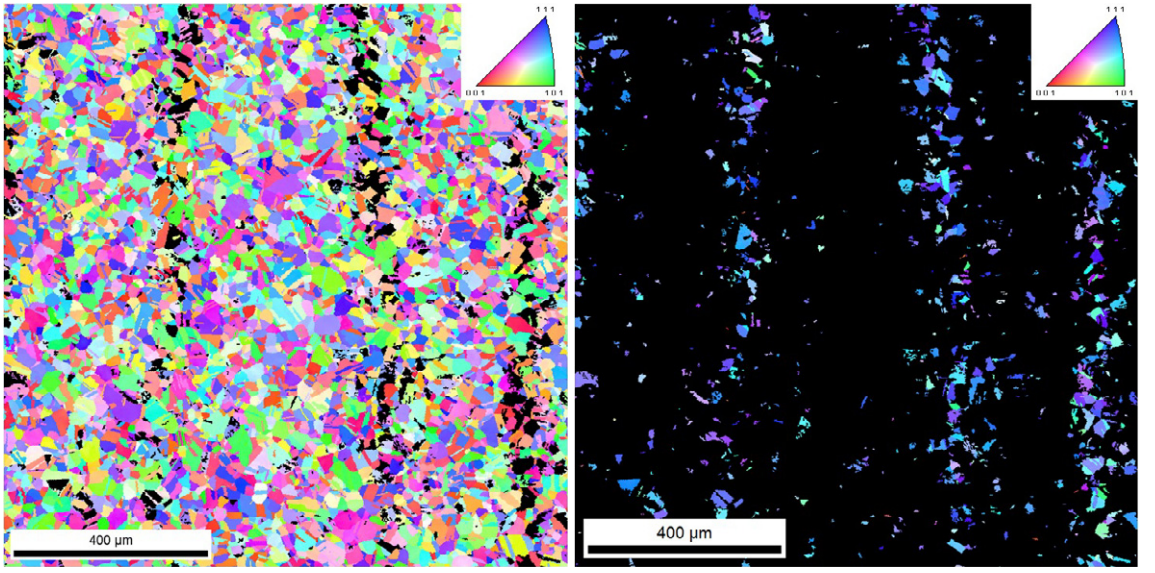

(a) Orientation and grain size of austenite (fcc). (b) Orientation and grain size of ferrite (bcc).

Fig. 1. Microstructure of initial material. Both figures show the same section of material, which is 92.8% austenite. For example, in a), the austenite regions, color coded by orientation, are shown, and the black regions correspond to the ferrite grains. In b), the ferrite regions and orientation are shown, and the austenite is shown in black. Accordingly, the black portions of one figure correspond to the colored portions of the other figure. The ferrite is caused by coldworking during the extrusion, and the bands remaining are residual ferrite after the annealing process. The vertical ferrite bands shown are oriented parallel to the extrusion axis. The ferrite does not appear as bands in a transverse section.

2. Materials and Experimental Setup

The material used was obtained from Carpenter as annealed Kovar in the form of a cylindrical rod. The documentation received from Carpenter listed the composition as 53.06%Fe, 28.93%Ni, 17.44%Co, .24%Mn, .15%Cr, .13%Si, and the balance trace elements at .01% or less. The microstructure of the material was examined on a representative sample from the interior of the annealed Kovar bar using SEM + OIM (orientation imaging microscopy). The structure was found to consist of a major fraction (92-95%) of unoriented austenite (fcc), consistent with an annealed structure, with the remainder consisting of preferentially oriented ferrite (bcc). The OIM micrographs are shown in Figure 1. The average grain size was ~20 μm (70% area fraction was covered by grains of diameter 10-30 μm), with a hardness of 86±1 HRB. Sections from the transverse direction were similar, indicating a well-annealled sample. The ambient ultrasonic sound speeds were measured and found to be 5.09±.04 km/s and 2.45±.02 km/s for the longitudinal c_L and shear c_S wavespeed respectively, yielding a bulk soundspeed c_B of 4.23 km/s and Poisson's ratio ν of .35. The density of each sample used in the experiments was determined using the mass and measured dimensions and found to be 8.16-8.17 g/cc except for one sample at 8.13 g/cc. The reason for the slight outlier is not clear. An averaged density of 8.16 g/cc was used for all calculations.

All experiments were conducted on a 60mm bore, single stage powder gun located at Eglin Air Force Base. The experiments were symmetric planar impact, using one of two different setups. In some setups (hereafter termed "dual target" setups), a thin (nominally 1.5mm) impactor was launched into a dual-thickness target (nominally 3 and 6mm), where the rear free surface of each target was monitored with VISAR. In the dual target setups, the diameter of the 3mm target was 17mm, and the effective diameter of the 6mm target was 27mm. In the "single target" setups, the impactor and target was 4mm and 6mm thick, respectively, and the diameter of all targets was 44mm. In both setups, the diameter of the impactor was 55mm, and the impactor was backed by a disc of TPX. The impact velocity and tilt were measured using

Table 1. Experimental matrix for Kovar.

Shot	Impactor [mm]	Target 1 [mm]	Target 2 [mm]	V_{impact} [km/s]
19	1.500	3.003	5.978	0.381
20	1.497	3.000	5.972	0.766
21	1.498	3.002	5.974	1.204
22	3.955	5.974	-[1]	1.534
23	3.970	5.974	-[1]	1.994
43	1.498	3.001	5.975	1.697
44	1.499	3.002	5.978	2.277

[1] Only one target was used.

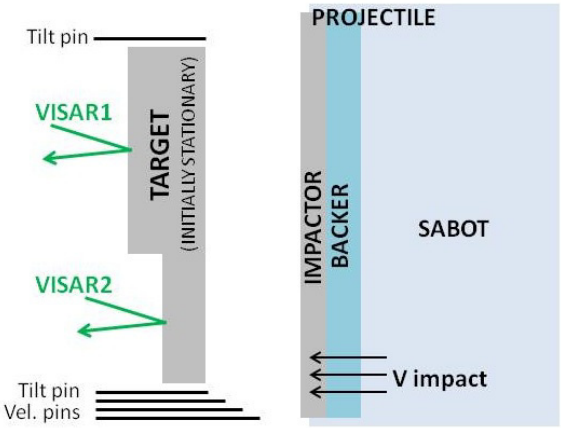

Fig. 2. Experimental Setup. The dual target setup is shown.

self shorting pins positioned around the sample. A schematic of the experiment is shown in Figure 2. The experimental configurations and impact conditions are detailed in Table 1.

3. Results

Traces were obtained from all experiments and are shown in Figure 3. For each of the dual-target experiments, the data is presented as two experiments- one with the "short" (thin) target and one with the "long" (thick) target. For example, the data corresponding to the thin, short target in experiment 19 is referred to as shot 19S, whereas the data corresponding to the long target is referred to as shot 19L. From symmetry, the particle velocity U_P is half the impact velocity. In experiments with an observed elastic precursor, the time of impact was calculated using the precursor as a time fiducial. In the overdriven single target experiments (shots 22 and 23), the tilt pins were used to determine impact time. In both cases, the impact time was then used to calculate the shock speed U_S. For the overdriven dual target experiments (shots 43 and 44), the difference in sample heights and tilt-corrected arrival times were used to calculate U_S, and then U_S was used to calculate impact time. It can be seen that even in the underdriven experiments, there was no well defined Hugoniot Elastic Limit (HEL). Instead a ramped behavior is observed in all experiments. The change in free surface velocity due to the HEL, $\Delta U_{fs,HEL}$, was assigned by intersecting lines fitted to the initial, steeper elastic rise and the gradual rise behind it. For these experiments $\Delta U_{fs,HEL}$ was about 30 m/s, corresponding to a stress σ_{HEL} of 0.6 GPa. For shot 19, the plastic wave shows a slow but finite rise, and so the arrival of the "shock" wave was taken at the steepest point of the rise, as determined by smoothing the

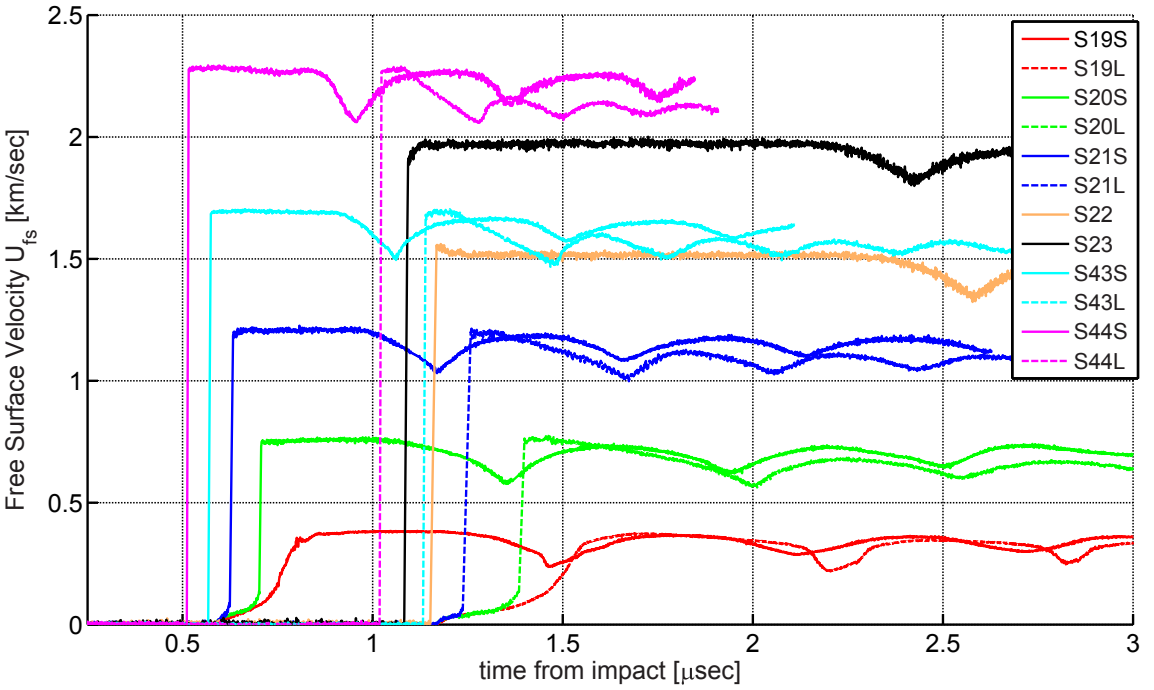

Fig. 3. VISAR traces from all experiments.

curve, differentiating, and taking the point at the maximum. For all other experiments, the shock wave arrival was taken as the instant the VISAR fringes became too fast to be resolved (or, equivalently, at the beginning of the steep jump shown in the traces). In shot 22 a very unusual overshoot and decay was observed after arrival of the shock. We believe that the actual material response for S22 is similar to that shown for S23, but have shown the recorded trace here for completeness. This overshoot and decay is hereafter ignored. The value of the Hugoniot stress σ_{Hug} was determined by computing the incremental stress change along the velocity profile as $\Delta\sigma = \rho_0\, c_{lag}\, \Delta U_P$, where c_{lag} is the local Lagrangian wavespeed, and then summing to obtain a stress history. This technique is widely used to analyze isentropic loading data, and is equivalent to a step implementation of the Rankine-Hugoniot equations. The free surface approximation was used to relate ΔU_P to the change in free surface velocity. The Hugoniot values are given in Table 2.

As previously mentioned, in all of these experiments the impactor was backed by TPX, a low-impedance polymer. Therefore, a spall plane was created in the sample as a result of the interaction of the tensile waves generated at the TPX/impactor interface and at the rear free surface of the sample. In each experiment, a spall signal is clearly visible in the velocity traces. The "pullback signal" ΔU_{pb} is the magnitude of the drop in the free surface velocity, and is given in Table 2. For symmetric impact experiments such as these, where the velocity is recorded on a free surface, the spall strength σ_s is most simply calculated as $\sigma_s = \rho_o c_{pb} \Delta U_{pb}/2$, where c_{pb} is the Lagrangian wavespeed of the pullback signal. This method of determining spall strength assumes that the entire pullback signal is traveling at the same velocity c_{pb}. If c_{pb} is assumed to equal c_L, the spall strengths $\sigma_{spall,simple}$ can be calculated and are shown in Table 2. This analysis is sometimes known as the acoustic approximation. A second estimation of the spall strength can be determined in a manner analogous to that described earlier for calculating the Hugoniot stress, such that the velocities c_{pb} and ΔU_{pb} are calculated incrementally and summed. This method relaxes the assumption that all components travel at the same velocity. The velocity c_{pb} is calculated from the known arrival time of the shock at the rear of the impactor, and assumes a constant release wavespeed through the impactor and target. Therefore, the calculated wavespeed neglects the effects of the release from the free surface of the target, and represents a lower bound of the actual release wavespeed. This is more clearly illustrated later in the x-t diagram of Figure 5(a) as characteristic BE. If the computed release wave velocities are compared with the ambient c_L,

Table 2. Experimental results.

Shot	U_P [km/s]	U_S [km/s]	σ_{Hug} [GPa]	ΔU_{pb} [km/s]	$\sigma_{spall,simple}$ [GPa]	$\sigma_{spall,comp}$ [GPa]	h [mm]	$\sigma_{spall,corr}$ [GPa]	$c_{L,Eul}$ [km/s]
19S	.191	3.911	6.35	.142	2.95	2.6	1.54	3.6	5.58
19L	.191	3.940	6.29	.152	3.16	2.7	1.52	3.6	5.34
20S	.383	4.272	13.3	.176	3.66	3.5	1.45	4.1	6.73
20L	.383	4.312	13.5	.190	3.95	3.9	1.36	4.3	6.17
21S	.602	4.814	23.7	.173	3.59	4.1	1.22	4.8	6.60
21L	.602	4.828	23.4	.186	3.86	4.7	0.97	5.0	6.52
22	.767	5.129	32.0	.176	3.66	4.0	3.14	5.5	6.70
23	.997	5.527	44.2	.150	3.12	3.7	2.93	5.2	6.88
43S	.848	5.273	36.4	.188	3.91	4.8	1.12	6.0	7.08
43L	.848	5.273[1]	36.4[1]	.211	4.38	5.8	0.76	6.2	6.91
44S	1.138	5.870	54.5	.212	4.40	6.0	0.97	7.1	7.42
44L	1.138	5.870[1]	54.5[1]	.215	4.47	7.0	0.58	7.4	7.43

[1] For shots 43 and 44, a dual target setup was used, but both targets were used to determine U_S (and therefore σ_{Hug}). Therefore, the U_S and σ_{Hug} listed are not independent measurements and are merely repeated in the table.

it is found that the computed speeds of the leading edge of the release fan are up to 34% higher than ambient c_L. Considering that these computed speeds are the lower limit, the actual wavespeeds are even higher. However, the speed decreases through the fan and in the case of the lower pressure shots can drop below ambient c_L at the trough of the pullback signal, cancelling some of the effect of the higher leading edge velocity on the calculated spall strength. Regardless, such a computed analysis represents a lower bound on the spall strength, and is listed in Table 2 as $\sigma_{spall,comp}$. Upon comparison with $\sigma_{spall,simple}$, it is clear that the values are significantly different except in the case of shot 20, where the weighted average computed (minimum) wavespeed happens to approximately equal the ambient wavespeed c_L.

The spall data can be further analyzed by correcting for the attenuation of the pullback signal as it travels through the target. The attenuation is due to the compressive wave generated from the spall plane travelling through the material at the elastic wavespeed and overtaking the characteristics in the (yielded) tension fan. A geometrical correction methodology has been used previously [4] and assumes only that the portion of the pullback signal which has been attenuated is a linear extrapolation of the remaining pullback signal ($\partial\sigma/\partial t$ must have remained constant). The correction $\Delta\sigma$ is given as Equation 1, where $\partial\sigma/\partial t$ is the stress release rate just before the pullback signal ends, h is the thickness of the spalled piece, and c_B and c_L are the bulk (plastic) and longitudinal elastic wavespeeds of the material in a state of tension just prior to spall.

$$\Delta\sigma = \frac{h}{2}\left(\frac{\partial\sigma}{\partial t}\right)\left(\frac{1}{c_B} - \frac{1}{c_L}\right) \tag{1}$$

Insufficient information is known about wavespeeds in the tensile state to precisely determine the last term. However, we assume that the ambient values can be substituted. This is not unreasonable since small strains are involved. The thickness of the spalled piece h was determined by measuring the period of the second reverberation of the spalled piece from the VISAR traces and using the measured ambient c_L. All thicknesses are shown in Table 2. Despite the calculated thickness of the spall layer for S19 being 2% larger than the impactor (a physically implausible result), we believe that these thicknesses provide the best estimates available. If these corrections are performed and applied to the values of $\sigma_{spall,comp}$ already presented, the corrected values of $\sigma_{spall,corr}$ can be computed and are given in Table 2. These corrected values give a remarkably consistent picture of spall strength increasing with pressure, with shot 23 as the only outlier. Furthermore, the correction brings the spall strength values from different sample thicknesses

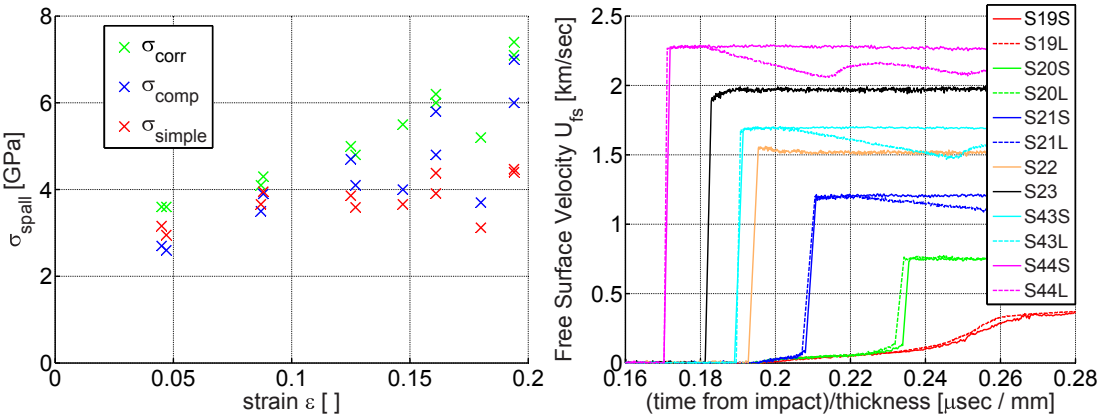

(a) Spall strength as a function of Hugoniot strain.

(b) VISAR traces with time normalized by the target thickness to highlight differences in wave propagation velocities.

Fig. 4. a) Spall strength and b) Normalized VISAR traces

into much better agreement. However, it should still be noted that by not correcting the wavespeed for the effects of the free surface of the target in the $\sigma_{spall,comp}$ calculation (see Figure 5(a)), even the $\sigma_{spall,corr}$ values represent a lower bound.

The spall data given in Table 2 is shown in Figure 4(a), plotted against volumetric strain at the Hugoniot state. Again, it is apparent that the method of computing σ_{spall} has a large influence. It is also apparent that the corrections are much smaller for the "long" samples. Furthermore, with the exception of the anomalous data point of shot 23, the data from both the corrected method and the computed method with long samples (likely to be the most accurate) clearly show increasing σ_{spall}.

The dual target experiments are useful to examine wave dispersion. Figure 4(b) shows the initial portion of the profiles shown in Figure 3, where the abscissa has been normalized by the thickness of the target. From this figure, the data indicates the apparent wavespeed is actually increasing, albeit slightly, as the sample thickness increases. Since we are currently unable to explain this observation, we take this result as an indication that the time-normalized profiles are essentially the same. For the ramp loading of shot 19, the profiles represent a centered wave, where the waveform is dispersing at a constant rate due to various components travelling at respective constant propagation velocities. The same logic applies to the ramp portions of shots 20 and 21. The shocks are non-dispersive, as the apparent slopes are artifacts of the VISAR analysis; the time over which the slope is present corresponds to the time during which the VISAR fringes were unresolved.

Sound speed at pressure can also be inferred from these experiments. The method is described here briefly. An x-t diagram of Shot 23 is shown in Figure 5(a). Upon impact, shock waves AC and AB propagate into the sample and impactor, respectively. Release fans are generated at both B and C, and so release waves propagate back into the impactor and target material. The leading edges of the fans are shown as black lines CD and BD, which propagate at the release velocity c_R, which is the longitudinal elastic wavespeed at elevated pressure. The leading edges of the release fans interact at point D. As the leading edge BD passes through the release fan represented by CD, it slows down until it reaches the ambient longitudinal wavespeed c_L (assuming that the material is relatively unaffected by the accumulated plastic deformation). The actual time the release wave reaches the free surface is known from the VISAR trace and is represented by point E. Therefore, a line corresponding to the leading edge of the release fan moving at c_L is constructed and shown as the red line DE. Then, c_R is iterated until the intersection of BD and CD lies on ED. If the dispersion in the release fan is considered, the velocities obtained in this way can be viewed as an upper bound to the true velocities, whereas the velocity corresponding to line BE (the uncorrected c_R) is the lower bound. This correction for c_R is larger as the distance from interaction point D to the probed surface EC increases. The

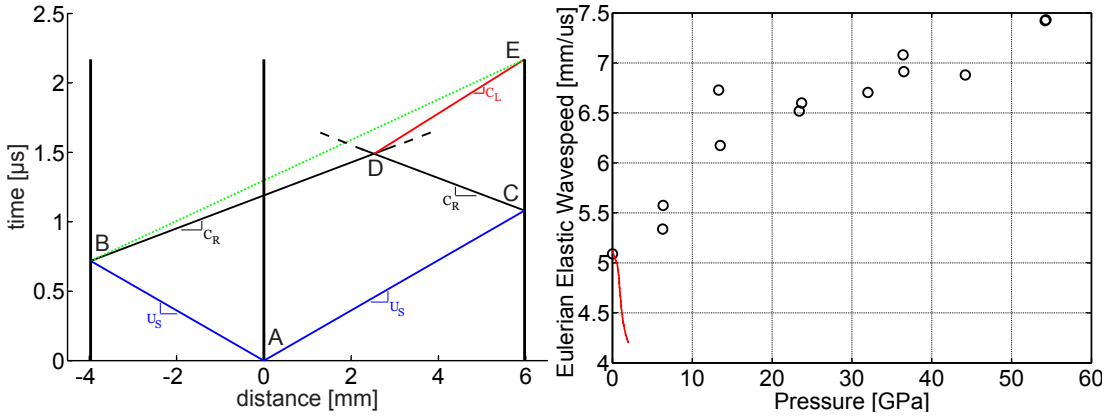

(a) x-t diagram for experiment 23, illustrating the method for estimating the sound speed at elevated pressure. Experiment 23 is chosen for illustration because the correction is large and easily seen graphically.

(b) Eulerian elastic wavespeed as a function of pressure. The red line is from the ramp loading portion of shot 19. The other points are from the release wave arrival in the VISAR traces, corrected by the method illustrated in (a).

Fig. 5. Release wavespeeds at pressure- method of determination and data.

correction is large for experiment 23, shown in Figure 5(a), and becomes smaller as the ratio of impactor to target thickness decreases. The corrected c_R values are then transformed to Eulerian coordinates, and are given in Table 2 as $c_{L,Eul}$ (Eulerian longitudinal soundspeed) and plotted in Figure 5(b). As expected, the speeds increase with pressure.

4. Discussion

The Hugoniot data is plotted in U_S-U_P space and shown in Figure 6. In Figure 6, the previously mentioned observation of the shock speed increasing slightly with propagation distance for the dual target experiments is apparent on the three lowest pressure experiments. The points are reasonably linear, as illustrated by the dashed line. The lower-pressure Kovar data of Wise et al.[1], performed with a similar setup (Kovar symmetric impact, 1.6mm impactors, 3mm targets, VISAR on rear free surface) is also shown. While the data of Wise et al. shows a negative slope and the data from the present work shows a positive slope, it is satisfying that the two data sets agree very well where they approach each other. Furthermore, the waveforms reported by Wise et al. match the waveform of experiment 19S, including the risetime, structure of the rise, and structure in the spall pullback signal. The only exception is the elastic precursor: in the work of Wise the precursors are much more defined than in this work and they are of significantly higher magnitude. Wise reports $\Delta U_{fs,HEL}$ values of 45-50 m/s, whereas we observed values around 30 m/s in this work, leading to lower values of σ_{HEL}. This discrepancy indicates a difference in initial material condition. Although material specifications were reported in the work of Wise et al., it appears that the values were specifications for Kovar from the foundry, rather than measured values for the tested material, making it difficult to speculate on the reason for the differences in the elastic precursor. The calculated sound speeds from the "ramp" portion of the loading wave prior to the jump (for the experiments that were not overdriven) are also plotted in Figure 6. Again, it is gratifying to find the calculated speeds approach the shock velocities reported by Wise et al. Comparing the spall strength with that reported previously, Wise et al. reports a value of 3.13 GPa for the highest pressure tested. The exact method used to compute the value is not known, but from analyzing the data traces it appears the simple method was used. In this work with 3mm target thicknesses (the same thickness as that used by Wise), the simple method on experiment 19S yielded a spall strength of 2.95 GPa, as shown in Table 2. Although this is reasonably good agreement (within 6%), without additional data it is impossible to say whether the difference is due to material behavior, as in the case of the elastic precursor, or simply to experimental scatter.

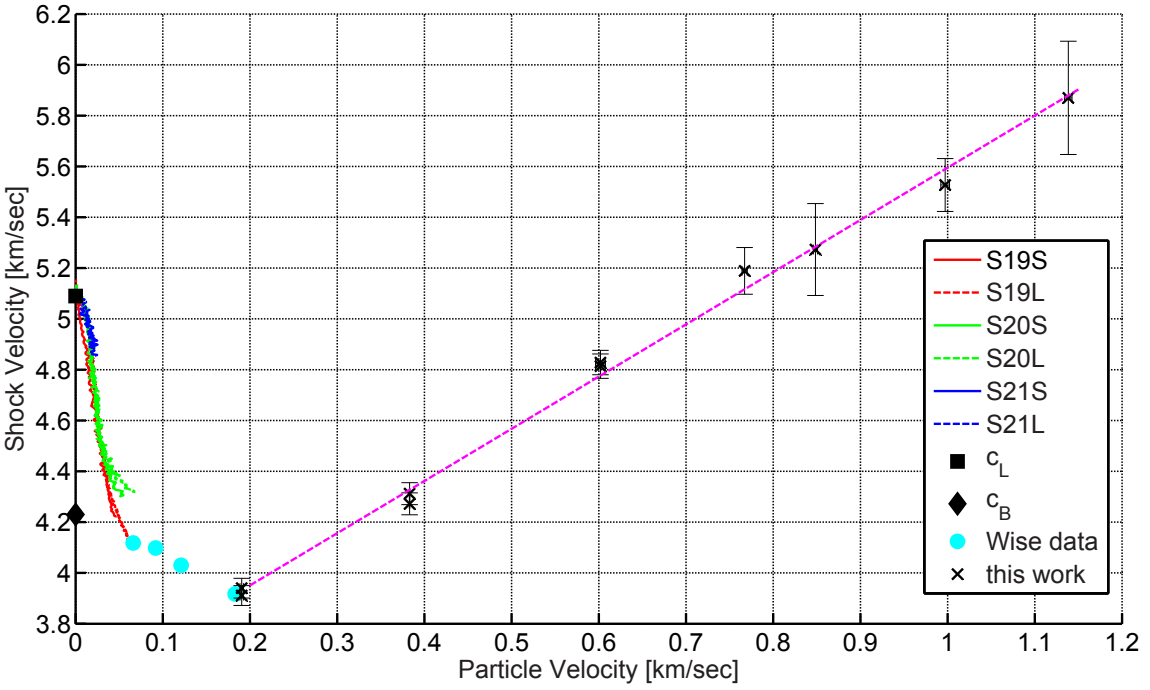

Fig. 6. U_S-U_P Hugoniot data for this work as well as the lower pressure Kovar data of Wise et al.[1]. The ramp loading portions of shots 19-21 are also shown. Note the agreement between the initial, ramp loading portion of shot 19 and the data of Wise, and also the agreement between the lowest pressure data of this work and the highest pressure data of Wise. The dashed line shown is a linear fit to the data of this work corresponding to $U_S = 3.54 + 2.06U_P$.

As indicated in Table 2, σ_{spall} varied with σ_{Hug}. Such a dependence of spall strength has been reported for some metals in the literature [5, p.225], where the dependence is attributed to strain hardening. However, in other references [6, p.144] the variation of σ_{spall} is attributed to a dependence on strain rate $\dot{\epsilon}$ during the tensile loading leading up to the spall fracture. In that work, the authors report that a power law of the form $\sigma_{spall} = A\dot{\epsilon}^m$ can be used to describe the spall strength across a range of strain rates. However, our data does not follow the power law, and does not collapse into any meaningful pattern when any of the σ_{spall} data is plotted against $\dot{\epsilon}$. Therefore, we attribute the $\sigma_{spall}(\sigma_{Hug})$ dependence to strain hardening (hence the use of strain as the abscissa in Figure 4(a)), although we acknowledge that since the experiments were not designed to independently vary strain and strain rate, it is difficult to be sure of the underlying σ_{spall} dependency.

Regardless, the combination of the data presented here and that reported previously[1] gives an consistent picture of Kovar behavior. The material displays an anomalous Hugoniot, where at low pressure the criterion for stability, $(\partial^2 P/\partial V^2)_s > 0$, is not satisfied. Above $U_P \approx 0.2\ km/s$, a normal Hugoniot is observed, but extrapolates to a bulk sound speed 16% below the ambient value obtained from ultrasonic measurements. Further evidence of the anomalous low pressure behavior can be found in the traces of Figure 3. The lowest pressure experiment, S19, shows pronounced structure in the unloading trace which is less clearly seen in experiment 20 and is completely absent from the other, higher pressure experiments. The structure is indicative of a rarefaction shock caused by either a phase reversion or by an anomalous Hugoniot. Wise et al, in addition to performing free-surface spall experiments yielding data very similar to our experiment 19, also performed window experiments using sapphire to approximate an in-situ measurement. The profiles clearly show unloading behavior indicative of a release shock. The reason for the transition from anomalous to normal behavior is not clear. In the compendium of Marsh[7], data for several Fe-Ni alloys are listed from pressures of about 40 GPa and higher, and each of them fails to extrapolate to the ambient bulk sound speed, indicating that high nickel content in Fe alloys may cause anomalous behavior. One Fe-Co alloy (Fe-40Co) is given in that work, which shows a clear phase transition beginning at about

40 GPa, but below the phase transition the data extrapolates to the bulk soundspeed, indicating the absence of a phase transition below 40 GPa.

To date, little work has been reported in the literature examining the effect of Ni or Co on the well known 13 GPa α (bcc) $\rightarrow \epsilon$ (hcp) pressure induced phase transition[3]. Although some stainless steels containing high Ni content (such as type 304, with ~10% Ni) have been investigated, because the predominant phase is austenite (fcc) no transition is observed [8, 9], and so inferring the effect of Ni on the bcc $\rightarrow$ hcp transition is difficult. Investigations have primarily focused on low alloy content steels, where the effect on the phase transition has been minor. There are a few exceptions. A single experiment was performed on a meteorite sample composed of 7.5wt% Ni, 0.4wt% Co, and the remainder Fe at pressures above the phase transition[10]. The material, though mixed phase, was 70-80% bcc, with most of the remainder fcc. However, the bcc phase was reported as the "nickel poor" phase. Is it therefore not surprising that the phase transition pressure reported (13.9 GPa) was similar to that reported for pure iron. Several impact experiments were reported on 6.8wt% Mn, 6.43wt%Ni, Fe alloys [11, 12]. Although microstructural details are not given, the authors report an $\alpha \rightarrow \epsilon$ transition stress of 6-7 *GPa*- a decrease of 50% from the accepted value for pure bcc iron. In older work, a systematic study to understand the effect of alloying on the transition in iron revealed that increasing the content of Ni in a binary Fe-Ni alloy strongly decreased the transition stress[13]. In another study, a binary alloy of 36wt%Ni and Fe ("Invar") was investigated [14] down to 3.5 *GPa* and no phase transition was observed. However, that investigation did indicate that the transition pressure decreased as the concentration of Ni increased, and suggested inconclusively that Invar might transition at 1-1.5 GPa, below the lowest data point of the experimental series. From this limited data it seems clear that Ni lowers the $\alpha \rightarrow \epsilon$ transition pressure. As for Co, the previously mentioned findings of Loree et al.[13], in addition to the effect of Ni, also showed that increasing Co increased the transition stress. Furthermore, the Fe-40Co data listed in the Marsh compendium[7] indicates a transformation at around 40 GPa (which we speculate is the $\alpha \rightarrow \epsilon$ transition). From this limited data, it appears that Co raises the $\alpha \rightarrow \epsilon$ transition pressure.

Additional insight on the effect of Ni and Co can be gleaned from the metallurgical literature, which for the Fe-Ni-Co system primarily deals with ambient pressure phase diagrams involving α and γ rather than α and ϵ phases. Again, from work on stainless steels, it is known that as the nickel content of Fe-Ni increases, the bcc α phase becomes less thermodynamically favored [15, 16], at least at atmospheric pressures. Furthermore, although Ni and Co have similar atomic numbers, atomic weights, and atomic radii, in the Fe-Ni-Co system they act very differently to affect the equilibrium crystalline structure, as illustrated in the phase diagrams of Raghavan[17]. In fact, those phase diagrams show that Co is a weak α stabilizer (as opposed to Ni, which is a strong γ stabilizer). Although these observations do not neccessarily explain the effect on the α to ϵ phase transition, it does illustrate that despite the similarities, the two elements are unlikely to have the same effect on the transition.

The suggestion that making the α phase less favorable in equilibrium α-γ phase diagrams may lead to decreasing the $\alpha \rightarrow \epsilon$ transformation pressure therefore seems plausible, given that Co is an equilibrium α stabilizer and also raises the $\alpha \rightarrow \epsilon$ transition pressure, and Ni is an equilibrium α destabilizer and also lowers the $\alpha \rightarrow \epsilon$ transition pressure. We therefore seem to have competing mechanisms- nickel is likely to strongly lower the transition pressure, and cobalt is likely to weakly raise it. Unfortunately no information regarding the tendency to form the equilibrium hcp ϵ phase (as opposed to the non-equilibrium bct α' martensite) from α could be found for the Fe-Ni-Co ternary system. However, for the above reasons, and due to the greater nickel content, we believe that the transformation pressure in Kovar will be significantly lowered. From the present work, even with only 5-8 vol% ferrite, and also from the evidence suggesting a lowered transition pressure with such high Ni content, we believe that no phase transformation is present in the range of 6-55 *GPa*, even though such a transformation in our material would appear as dispersion in the loading profile rather than as a classic dual-wave structure. If a transition is present from 2.4-6 *GPa*, it should be evident in the work of Wise if an appreciable fraction of ferrite was present in their samples (the phase composition was not reported). Although some of the loading and release profiles in that work are suggestive, no conclusive evidence of the transition is found in that study. Whether this is due to an absence of such a transition within the range investigated, or due to insufficient ferrite material in the samples, is unknown. Further work, ideally with material cold-worked to obtain a high fraction of ferrite and individually characterized,

is needed to investigate whether or not Kovar undergoes a phase transformation at low pressures.

5. Conclusion

The Hugoniot and spall strength of Kovar are reported, and it is clear that Kovar displays anomalous shock behavior below a particle velocity of ~0.2 km/s. The tensile strength, as indicated by spall, increases dramatically across the range investigated, and it is shown that magnitude of the spall strength is highly dependent on the assumptions made in the analysis technique. We suspect a low-pressure phase transformation is the cause of the anomalous behavior, and show that the shock and metallurgical literature, while not conclusive, do suggest that a low pressure phase transformation might be responsible. Further study with carefully characterized material is needed to understand the low pressure behavior.

6. Acknowledgements

We are grateful to Adam White and Rick Davis for experimental preparation, setup, and execution, to Bill Peaden for skillful fabrication on short notice, and to Cadet Kelsey Collier for metallurgical sample preparation and imaging.

References

[1] J. Wise, S. Jones, C. Hall, J. Asay, D. Sanchez, Dynamic response of kovar to shock and ramp-wave compression, in: Shock Compression of Condensed Matter - 2007, 2007, pp. 1204–1207.
[2] D. Bancroft, E. Peterson, S. Minshall, Polymorphism of iron at high pressure, Journal of Appied Physics 27 (1956) 291–298.
[3] L. Barker, R. Hollenbach, Shock wave study of the alpha - epsilon phase transition in iron, J Appl Phys 45 (1974) 4872–4887.
[4] V. Romanchenko, G. Stepanov, Dependence of the critical stresses on teh loading time parameters during spall in coper, aluminum, and steel, Zhurnal Prikladnoi Mekhaniki i Tekhnicheskoi Fiziki (4) (1980) 141–147.
[5] M. Zhernokletov, B. Glushak (Eds.), Methods for Study of Substance Properties Under Intensive Dynamic Loading, Federal Governmental Unitary Enterprise, 2004.
[6] T. Antoun, L. Seaman, D. Curran, G. Kanel, S. Razorenov, A. Utkin, Spall Fracture, Springer-Verlag, New York, 2003.
[7] S. P. Marsh (Ed.), LASL Shock Hugoniot Data, University of California Press, Berkeley and Los Angeles, CA, 1980.
[8] G. McQueen, S. Marsh, J. Taylor, J. Fritz, W. Carter, The Equation of State of Solids from Shock Wave Studies, High Velocity Impact Phenomena, Academic, New York, 1970.
[9] T. Duffy, T. Ahrens, Dynamic compresion of an fe-cr-ni alloy to 80 gpa, Jounal of Applied Physics (9) (1997) 4259–4269.
[10] M. Furnish, M. Boslough, G. Gray, J. Remo, Dynamic properties measurements for asteroid, comet and meteorite material applicable to impact modeling and mitigation calculations, Internation Journal of Impact Engineering (1995) 341–352.
[11] Z. Tang, X. Tang, X. Zhang, H. Hu, W. Xu, Abnormal spall behavior observed in pure iron and femnni alloy undergoing a-e phase transition, in: Shock Compression of Condensed Matter - 2005, 2005, pp. 662–665.
[12] C. Yongtao, H. Haibo, T. Xiaojun, L. Qingzhong, P. Qixian, H. Jianbo, Phase transition behavior and abnormal spall in femnni alloy with low a-e transition stress, in: Shock Compression of Condensed Matter - 2007, 2007, pp. 493–496.
[13] T. Loree, C. Fowler, E. Zukas, F. Minshall, Dynamic polymorphism of some binary iron alloys, Journal of Appied Physics 37 (1966) 1918–1927.
[14] D. Curran, On the possiblility of detecting shock-induced second-order phase transitions in solids. the equation of state of invar, J Appl Phys 32 (1961) 1811–1814.
[15] V. Raghavan, User applications of alloy phase diagrams, Transactions of The Indian Institute of Metals 62 (2009) 1–9.
[16] F. Pickering, Physical metallurgy of stainless steel developments, International Metals Reviews December (1976) 227–268.
[17] V. Raghavan, Co-fe-ni (cobal-iron-nickel), Journal of Phase Equilibria 15 (1994) 526–527.